ADVANCED FUNCTIONAL MATERIALS
www.afm-journal.de

Real-Time IR Tracking of Single Reflective Micromotors through Scattering Tissues

Azaam Aziz, Mariana Medina-Sánchez, Nektarios Koukourakis, Jiawei Wang, Robert Kuschmierz, Hannes Radner, Jürgen W. Czarske, and Oliver G. Schmidt**

Medical micromotors have the potential to lead to a paradigm shift in future biomedicine, as they may perform active drug delivery, microsurgery, tissue engineering, or assisted fertilization in a minimally invasive manner. However, the translation to clinical treatment is challenging, as many applications of single or few micromotors require real-time tracking and control at high spatiotemporal resolution in deep tissue. Although optical techniques are a popular choice for this task, absorption and strong light scattering lead to a pronounced decrease of the signal-to-noise ratio with increasing penetration depth. Here, a highly reflective micromotor is introduced which reflects more than tenfold the light intensity of simple gold particles and can be precisely navigated by external magnetic fields. A customized optical IR imaging setup and an image correlation technique are implemented to track single micromotors in real-time and label-free underneath phantom and ex vivo mouse skull tissues. As a potential application, the micromotors speed is recorded when moving through different viscous fluids to determine the viscosity of diverse physiological fluids toward remote cardiovascular disease diagnosis. Moreover, the micromotors are loaded with a model drug to demonstrate their cargo-transport capability. The proposed reflective micromotor is suitable as theranostic tool for sub-skin or organ-on-a-chip applications.

1. Introduction

Medical untethered micromotors are engineered small devices which can move in biological environments by chemical reactions,[1–6] external physical fields[7–15] or by motile cells and/or microorganisms.[16–19] They come in different shapes, one of the most prominent ones being particle micromotors,[20] which have been used to demonstrate different motion mechanisms. Micromotors are designed to perform functions such as active targeted drug delivery,[18,21–28] assisted fertilization,[10] microsurgery,[29–31] or sensing.[32,33] However, the control and visualization of such micromotors to perform medically relevant tasks remain key challenges.[34] A micromotor always possesses a synthetic component, which apart from its original function (e.g., cargo-delivery, guidance, or cell capture), can be used itself as a contrast agent for imaging or be functionalized with emitting or absorbing reporters for enhanced visualization in complex environments. To date, various imaging techniques have been used for the tracking of micromotors,[29,35–37] in particular to visualize swarms of them.[21,38–40] However, the spatiotemporal resolution of such imaging techniques is insufficient to exert precise control over one or few micromotors in deep biological tissues in real-time.

Ultrasound (US), for instance, offers imaging deep inside living tissue and enables real-time tracking but provides insufficient spatial resolution to track microsized objects and lack on molecular specificity. An in vitro study has shown real-time tracking of a trail of microscopic bubbles from a fast-moving

A. Aziz, Dr. M. Medina-Sánchez, Dr. J. Wang, Prof. O. G. Schmidt
Institute for Integrative Nanosciences
Leibniz IFW Dresden
Helmholtzstrasse 20, 01069 Dresden, Germany
E-mail: m.medina.sanchez@ifw-dresden.de; o.schmidt@ifw-dresden.de
Dr. N. Koukourakis, Dr. R. Kuschmierz, H. Radner, Prof. J. W. Czarske
Chair of Measurement and Sensor System Technique
School of Engineering
TU Dresden
Helmholtzstrasse 18, 01069 Dresden, Germany
The ORCID identification number(s) for the author(s) of this article can be found under https://doi.org/10.1002/adfm.201905272.

DOI: 10.1002/adfm.201905272

Prof. J. W. Czarske
Cluster of Excellence Physics of Life
TU Dresden
01069 Dresden, Germany
Prof. O. G. Schmidt
Research Center for Materials
Architectures and Integration of Nanomembranes (MAIN)
Rosenbergstraße 6, TU Chemnitz, 09126 Chemnitz, Germany
Prof. O. G. Schmidt
School of Science
TU Dresden
01062 Dresden, Germany

microjet engine using US with a spot size of ≈300 µm.[36] Magnetic resonance imaging (MRI) is suitable for submillimeter resolution but has limited temporal resolution for real-time monitoring of micromotors and demands complex infrastructure. For example, a swarm of naturally occurring *Spirulina platensis* micromotors was imaged in living mice using MRI,[41] at a temporal resolution of ≈0.2 frames per minute. Likewise, a swarm of magnetotactic bacteria used to deliver drug-loaded nanoliposomes to a tumor in mice was monitored using the same technique.[27] Nuclear imaging techniques, like positron emission tomography (PET) and single photon emission computed tomography in combination with computed tomography (CT),[42] offer high sensitivity and molecular information,[43] but utilize ionizing radiation which could be a drawback if prolonged radiation is needed to observe the micromotors while controlling them for long periods of time.[42,43] PET in combination with anatomical techniques such as CT was used to track a cluster of catalytic micromotors labeled with radioactive isotopes in transparent glass tube phantoms.[35] Recently, metal-coated microparticles were propelled and visualized using X-ray irradiation in aqueous solution in real-time.[37] The extended X-ray exposure to the tissues can be harmful to guide the micromotors to the region of interest. Fluorescence imaging was also used to track a swarm of artificial bacterial flagella in vivo,[40] as well as a cluster of autofluorescent *Spirulina platensis* micromotors, but at a very limited spatial and temporal resolution.[44] The figure of merit (Figure S1a,b, Supporting Information) compares the state of the art regarding the tracking of micromotors toward in vivo applications, using different imaging techniques, considering key parameters such as tracking speed, penetration depth, smallest imaged feature, imaging system complexity, and safety.

Optical imaging (OI) techniques have rarely been used to track micromotors due to limited penetration depth and pronounced photon scattering in biological tissues. However, in comparison with other imaging modalities, OI offers high spatial resolution and good sensitivity, which is equally important for real-time monitoring of medical micromotors and micro-scale dynamic processes. Prominent techniques like two-photon fluorescence microscopy, optical coherence tomography, and confocal microscopy all offer good depth discrimination due to their optical sectioning ability. However, the techniques acquire data pointwise and thus require scanning in three dimensions, which strongly limits image rates, making them unsuitable for real-time tracking. The penetration depth of most optical techniques is still limited to hundreds of micrometers or in some cases slightly beyond 1 mm in real biological tissues but only under static conditions and with prolonged exposure times, limiting investigations to sub-surface levels.[45,46] Fluorescence-based optical imaging relies on the well-known Jablonski energy diagram.[47] Fluorescent dyes or labels emitting in the IR decay over time and photobleach after encountering repetitive excitation processes.[48] Although quantum dots are more stable over time,[49] their detection requires prolonged acquisition times and are often constituted by toxic materials,[50–52] making them of limited use for applications in living organisms. There are few reports about the synthesis and study of biocompatible quantum dots.[53–57] Quantum dots have been employed to distinguish a cluster of cells,[58] molecules,[59] and specific proteins.[60] Still, such systems are extremely inefficient in providing feedback signal as their excitation cross-section is tiny and the re-emission signal is isotropic and not uni-directional. Therefore, most of the excitation signal is lost and real-time optical tracking of single or few micromotors below phantom or real tissue has not been reported to date.

The concept of reflectors was used as a nonspectroscopic optical immumosensing probe by utilizing silica particles (SiO_2, 1.2 µm in diameter). For that silica particles were functionalized with a specific antibody that recognizes a biomarker (cardiac troponin I) of acute myocardial infarction.[61] Likewise, Janus microspheres (polystyrene, 2 µm in diameter, 7.6×10^7 mL) were used as reporters to improve imaging contrast in optical coherence tomography in ex vivo mice liver and in vivo zebrafish.[62] In this work, we propose a new concept of reflective micromotor, driven by magnetic fields which can be visualized with high spatial and temporal resolution below scattering tissues. We have fabricated such micromotors by depositing a metal layer onto silica microparticles with diameters of 20 and 100 µm. As a proof of concept, we implemented a simple optical setup to visualize individual micromotors under ex vivo mouse skull tissues and tissue-mimicking phantoms using IR light with a wavelength of 970 nm over a large field of view, and demonstrated their applicability as microrheometers and as drug carriers.

2. Results and Discussion

2.1. Concept and Characterization of the Reflective Micromotors

Transparent silica particles can be converted into micro-reflectors by incorporating a thin gold layer as a biocompatible and highly reflective material.[63–66] Additionally, if we include a magnetic layer (Fe) into the reflective materials, we can control the position of the particles by external magnetic fields, resulting in magnetic reflective micromotors which can be steered and visualized under IR light. Layers of Au, Ti, Fe, and Au were deposited in series onto a monolayer of silica particles at an angle of 0°. Optical and scanning electron microscope (SEM) images show the asymmetric coating, leading to a semispherical cavity which is then used for imaging (**Figure 1**a-i,ii). Different deposition rates (0.5–1.0 Å s^{-1}) were used but no significant effect was observed on the roughness. Atomic force microscopy (AFM) analysis was carried out to determine the resulting roughness of the deposited metal surface (Figure 1b). The roughness within a 1 μm^2 area was calculated by the root mean square (R_q = 1.62 nm) and the maximum height feature ranges from −5 to 5 nm. Ideal reflection occurs on a surface with a roughness value of zero but in real cases, the reflected light possesses different path lengths due to reflection from different height locations, leading to diffuse reflection[67] and interference of the reflected light. The measured roughness (1.62 nm) of the gold surface is ≈0.17% of the used wavelength (975 nm) and hence guarantees a sufficiently good reflectivity.

The metal layers deposited on top of spherical transparent silica particles (⌀ = 100 and 20 µm) lead to a semispherical reflector to collimate the beam to an appropriate focus for their further visualization. The rear surface, exhibiting the Au/SiO*x* interface, acts as a concave spherical mirror and the incident light is reflected back internally through the leading surface of the micromotor and is being redirected back toward the light source[68,69] as indicated in

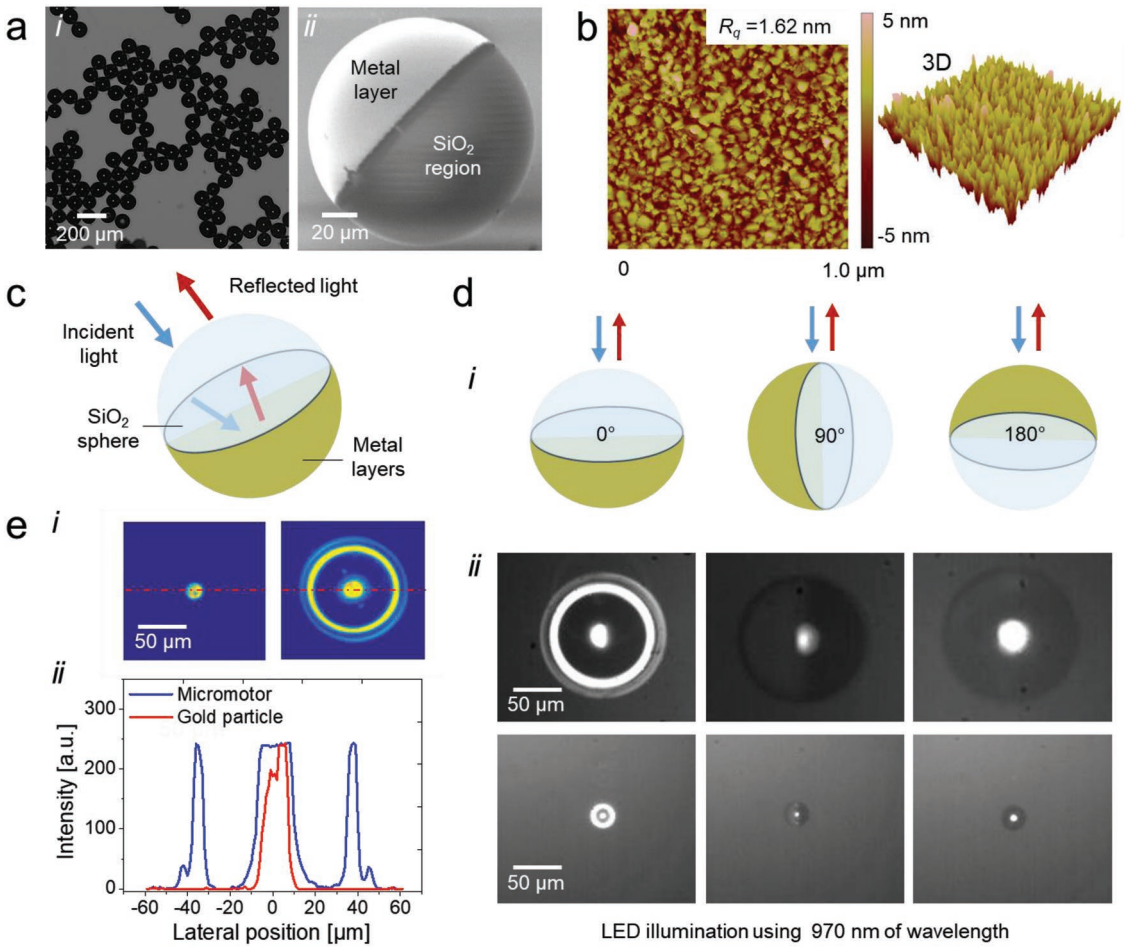

Figure 1. a) i) Bright-field microscopy image of a monolayer of metal-coated micromotors and ii) SEM image of a single micromotor showing the interface of the silica region and the evaporated layer surface. b) Surface morphology and roughness in 2D and 3D perspectives, revealing a root mean square roughness of 1.62 nm within a 1 µm^2 area. c) Concept and schematic of the reflective micromotor fabricated with silica particles half-coated with a metal layer. d) i) Schematic at different angles, and ii) the reflected light from the micromotors in different orientations (0°, 90°, and 180°) when irradiated with IR illumination (LED at 970 nm). e) i) Signal of the "reflective" micromotor and the "gold particle" of the same size and ii) their corresponding signal intensity distribution.

Figure 1c. The incident light, reaching the gold-coated surface of the reflective micromotor, eventually reflects back toward the light source along nearly the identical path.

The gold layer is highly reflective over a broad spectral range[70] and was chosen as a reflective layer coating half of the micromotor. The reflective micromotors can have different orientation angles as illustrated in Figure 1d-i. We distinguish between the "reflector" (0°), "gold particle" (180°), and "hybrid" (90°) orientation that can be controlled by applying the external magnetic field. The micromotors are illuminated by a light-emitting diode (LED) light source (center wavelength: 970 nm). The illumination source was held perpendicular to a fluidic channel and at different angles to the micromotor reflectors (Figure 1d-ii). The characteristic shape of the micromotor in the "reflector" orientation makes it easy to detect in comparison to a simple spot obtained by the "gold particle" configuration (Figure 1e-i). In case of the "gold particle" (same size like the "reflector"), the incident light scatters into a broader space angle with lower signal returning to the detector. The integral over the intensities shows that ≈13 times more light is reflected by the "reflector" compared to the "gold particle" (Figure 1e-ii). As previously demonstrated in the literature, such particle-based micromotors can be functionalized to carry drugs,[21] to guide bacteria,[71] or as a sensor for superficial disease diagnosis.[20] Therefore, we could envision a swimming micromotor, which not only serves to carry a cargo but also to perform local diagnosis or therapy while being visualized through scattering tissues using IR light.

2.2. In Vitro Tracking of Single Micromotors in Scattering Phantoms

The IR imaging system for real-time tracking is depicted in **Figure 2**a. The IR light (LED 970 nm) is collimated and directed toward the fluidic channel by the aid of an objective lens. A home-made C^{++} code was implemented to drive the InGaAs camera and process the data by subtracting the scattered background and using image cross-correlation-based algorithms to track the micromotors. The three axes stage is used to find the lateral position of the particle (*X*- and *Y*-direction) while the *Z*-axis is taken to readjust the focus position. With increasing thickness of the tissues, the focus position shifts

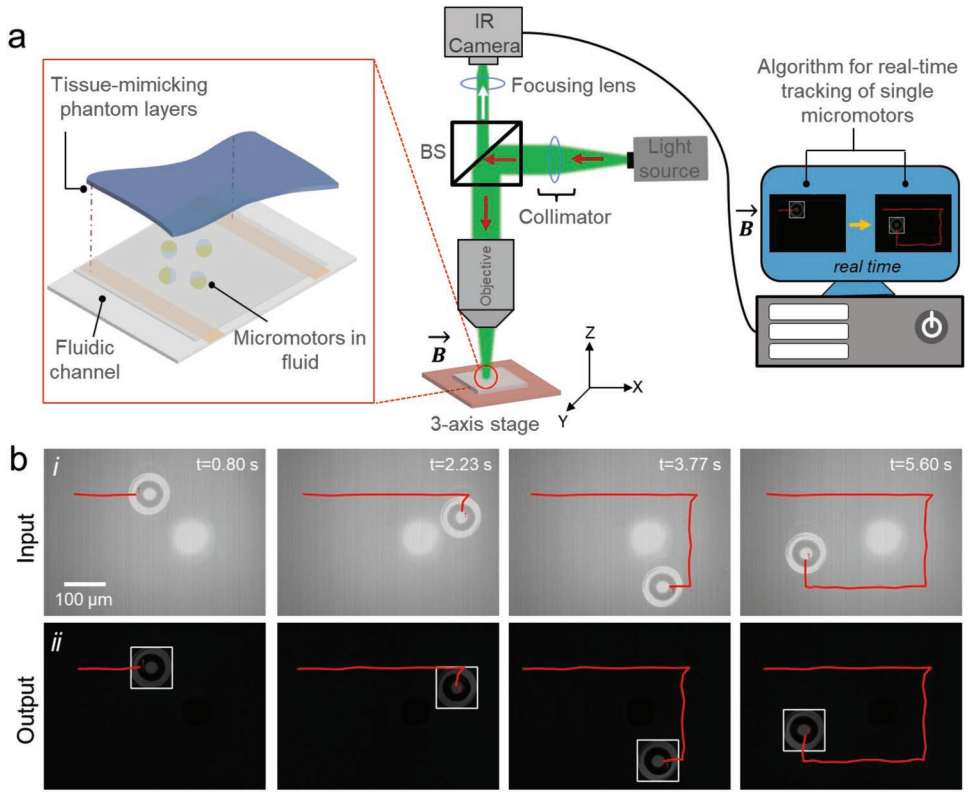

Figure 2. IR imaging setup and real-time tracking of single micromotors without any phantom or biological tissues: a) Schematic of IR imaging setup, inset: microfluidic channel containing micromotors and covered by scattering phantoms. b) Time-lapse images of a single bare micromotor (100 µm in diameter) tracked, i) before and ii) after algorithm implementation, along a rectangular trajectory without the scattering phantoms (from 0.80 to 5.60 s).

toward the objective, as the optical path length change, induced by the tissue, is the product of the local thickness and the refractive index. The phantoms were fabricated using a mixure of polydimethylsiloxane (PDMS) and glycerol. The phantoms were robust, easy to handle, and mimicked lung and bone tissues due to their similar structure.[72] The composition was thoroughly mixed and poured into petri dishes with controlled thicknesses (see the Experimental Section).

Prior to imaging, the micromotors were suspended in deionized (DI) water (≈10 µL) and injected into a fluidic channel (details in the Experimental Section). The orientation of the micromotors was controlled by an external magnetic field (≈20–25 mT). Two sizes of micromotors (100 and 20 µm in diameter) were imaged separately with and without scattering phantoms. Figure 2b summarizes the results from the dynamic imaging of the micromotors without scattering phantoms. Individual micromotors were tracked in real-time in an enclosed channel. Two separate windows indicate the tracking with unprocessed data (input) and with processed data (output, after real-time processing, Figure S2, Supporting Information). The complete trajectory of a single micromotor is depicted in the time-lapse images before and after implementing the real-time tracking algorithm (Figure 2b-i,ii). The central bright spot present in Figure 2b-i is an image of the LED and is part of the intensity, which is present in the system without any object, e.g., induced by internal back-reflections and camera noise. The central bright spot just influences and saturates a small part of the image and is removed in real time with a background intensity suppression algorithm, not affecting the results or the deduced limitations of the presented measurements.

In the first set of experiments, 1×1 cm^2 phantoms with thicknesses varying from 0.8 to 2.2 mm were prepared. Figure 3a,b shows the micromotors (100 and 20 µm in diameter) in the phantom tissues of varying thicknesses. As the lateral resolution of the imaging setup is <2 µm (Figure S3, Supporting Information), also smaller micromotors can be tracked. The experimental scenario is explained as follows: Light from the LED illuminates the phantom tissue. As the light is scattered, a diffused light field illuminates the micromotors. Using laser light would lead to a speckled illumination, meaning that the detected micromotor in "reflector" orientation would not show its complete characteristic ring shape, but varying arcs. Using LED light, instead, leads to a homogenous but diffuse illumination and background. The light is reflected from the micromotor and crosses the scattering tissue again. The signal strength collected by the camera depends on the thickness of the phantom tissues. The phantoms only mimic scattering properties of real tissues but their thicknesses do not correspond to the actual biological tissue thickness. This is due to the fact that the phantoms were prepared to be thicker but with less glycerol, maintaining the scattering properties while facilitating their handling for the experiments.

The physical parameters limiting the optical penetration depth in biological tissues are scattering and absorption, represented by the coefficients μ_s [m^{-1}] and μ_a [m^{-1}], respectively. The mean free path (MFP) is defined as the average distance

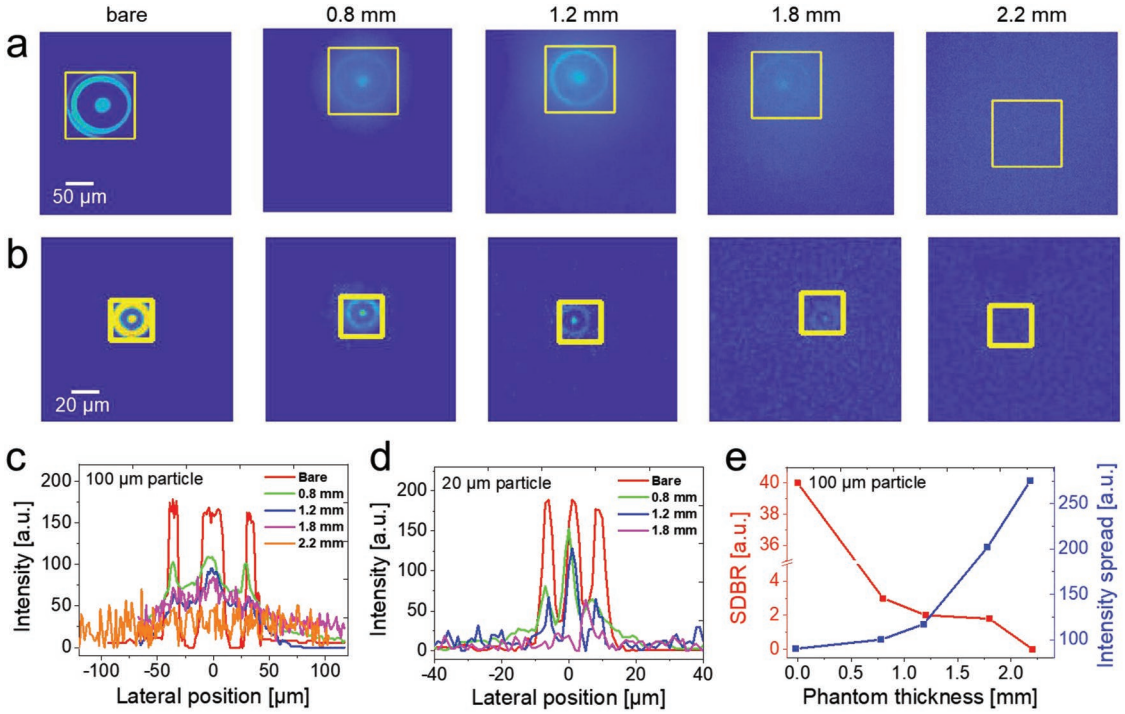

Figure 3. Tracking of a single micromotor beneath varying thicknesses of the scattering phantoms (0.8 to 2.2 mm in thickness) for a) 100 µm and b) 20 µm micromotor. c,d) Intensity profiles of the 100 and 20 µm micromotors, respectively. e) The SDBR decreases with increasing the phantom thickness (red curve) and is accompanied by an increase of the lateral intensity spreading (blue curve) due to increased amount of scattering of the diffuse light intensity back-reflected by the micromotors.

travelled by a photon between two scattering or absorption events.[45] Usually, the influence of absorption is small compared to scattering and the MFP only depends on the scattering coefficient according to MFP = $1/\mu_s$. However, the scattering in tissues is directional, which means that mainly forward scattering occurs, expressed by the anisotropy factor "g." The transport MFP (TMFP) takes into account the MFP and the average angle in which photons are scattered and is linked to the MFP by the reduced scattering coefficient μ_s' and TMFP = $1/\mu_s'$. The TMFP describes the average propagation distance a photon travels at which it has lost its direction information and can be called diffusive.[45] The scattering phantoms used here have an anisotropy factor of approximately $g = 0.975$[72] resulting in TMFP = 10 mm and MFP = 250 µm. See Table S1 in the Supporting Information to see the comparison of the used phantoms to various biological tissues.

The complete trajectories of a single micromotor (100 and 20 µm in diameter) are shown in Videos S1 and S2 in the Supporting Information, respectively. A maximum LED power density of ≈146 mW cm^{-2} for 2.2 mm thick phantom was used. This power density is within the allowed limits of exposure according to International Commission on Non-Ionizing Radiation Protection (ICNIRP) guidelines.[73] Both the 100 and 20 µm micromotors can be clearly distinguished in the processed images up to 1.8 mm thick phantom. With increasing phantom thickness, the characteristic features of the micromotor disappear in the diffuse background. The "reflective" micromotor has a characteristic reflection shape (concentric spot-ring geometry) that makes it easier to track in comparison to the single spot obtained by a simple "gold particle" (Figure 1c). We use image correlation between an ideal concentric spot-ring model and the real signal to recognize the particle position in each frame in real-time (Figure S2, Supporting Information). The increased scattering for increasing phantom thickness is documented by increased lateral spreading of the intensity at the camera. For 2.2 mm thick phantom, the characteristic features of the micromotors cannot be distinguished. However, the high reflectivity of the micromotors still leads to a strong but diffusive signal that moves with the particle still enabling its tracking. Due to rotational symmetry of the diffuse light, the lateral position can be securely detected. The axial position, however, is determined with higher position uncertainty. Using intensity or contrast analysis may help to improve.

The intensity profiles of the 100 and 20 µm micromotors at varying thicknesses of the scattering phantoms are displayed in **Figure 3**c,d, respectively. As the light power illuminating the micromotors is kept constant, mainly two effects that change with the phantom-thickness contribute to the detected signals. First, with increasing the scattering-phantom thickness the reflection efficiency of the micromotors is slightly reduced as the illumination takes place at a larger angular range. Second, the amount of scattering increases with phantom thickness, changing the intensity ratio between the intensity of the characteristic features of the micromotors and the diffuse signal, which leads to a reduction of the signal-to-diffuse-background ratio (SDBR) (red curve in Figure 3e). Concurrently, the lateral intensity spreading increases (blue curve).

The characteristic shape of the micromotor is visible up to a thickness of 1.8 mm, which corresponds to 0.18 TMFP. The

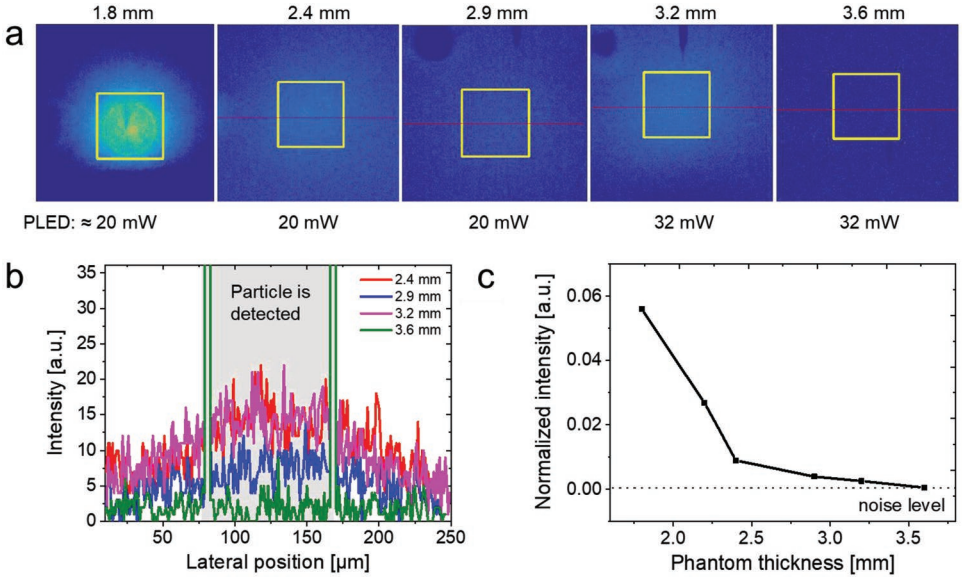

Figure 4. Micromotors beneath different phantom thicknesses: a) The micromotor is visible up to a thickness of 3.2 mm and it disappears for 3.6 mm. Note that the illumination power was strongly increased. Although the characteristic features of the micromotors are not visible, the lateral position of the micromotors can be securely detected due to the rotation symmetry of the diffuse light. b) Line scans across the lines marked in red. Up to a thickness of 3.2 mm, a clear signal from the micromotor is detectable, while for 3.6 mm it disappears in the noise. c) The relative intensity is obtained by dividing the integrated intensity of the background-subtracted images by the integrated background intensity.

upper experimental limit for the tracking of the diffuse signal is set by the dynamic range of the camera. The limitation of the imaging depth is governed by the saturation of the camera by scattered light, which depends on the camera properties like the dynamic range and sensitivity, as well as the employed exposure time, illumination intensity, and field of view. To probe this limit for our setup and phantoms, the phantom thickness was further increased under varying illumination conditions and the results are shown in **Figure 4**. The high reflectivity of the micromotor still enables to detect signals through 3.2 mm thick phantom, corresponding to 0.32 TMFP, whereas at 0.36 TMFP we only detect noise (Figure 4a). This can be observed in the line scans shown in Figure 4b. However, the line scans aim to show the limitation, not to really compare the line scans in terms of signal strength. The relative intensity is obtained by dividing the integrated intensity of the background-subtracted images by the integrated background intensity (Figure 4c). The illumination power was normalized by a simple correction factor.

2.3. Ex Vivo Tracking of Single Micromotors below Mice Skull Tissues

Real biological tissues have an anisotropy factor in the range of $g \approx 0.9$[74] and varying reduced scattering coefficients. 2 mm of the tissue-mimicking phantoms used in our studies correspond to 80–220 µm of real biological tissues (see Table S1, Supporting Information).

In this study, we replaced the phantoms by mice skull tissues to repeat the measurements. The skulls were taken from 8 and 14 days old mice. **Figure 5**a shows the mouse skull preserved in agarose gel to maintain their optical properties. First measurements were performed through the parietal bone of the skull. The thickness was estimated to be ≈80 µm for the 8th day and 90 µm for the 14th day skull. The micromotors were visualized underneath skull tissues as shown in Figure 5b (extracted from Video S3, Supporting Information). For both skulls, the characteristic shape of the micromotors was clearly visible. As a next step, the skull of the 14th day old mouse was shifted to the frontal bone part, which was estimated to be ≈110 µm thick. As can be seen, the characteristic shape of the micromotor disappeared due to scattering of the reflected photons through the skull tissues. However, as for the phantom tissues, still enough light is scattered back toward the camera and the position of the micromotor can be tracked. This is in good agreement with the results on the phantoms, considering Table S1 in the Supporting Information. The characteristic shape of the micromotor was visible up to a tissue-thickness of ≈0.2 TMFP. Figure 5c shows the intensity profile of the micromotors (100 µm) beneath varying thicknesses of the skull tissues.

Similarly, the smaller micromotor (20 µm in diameter) was captured (Figure 5d) and there was a moderate change in signal intensity by using the varying thicknesses of the tissues (see Video S4, Supporting Information). Figure 5e summarizes the intensity profile for 20 µm micromotors below the tissues of varying depths. As the smaller micromotors reflect less light, the characteristic shape disappears at 90 µm skull tissue.

2.4. Micromotors Moving through Viscous Fluids and as Drug-Carriers

Micromotors can be used for different medical tasks—most of them envisioned for targeted therapies. However, micromotors

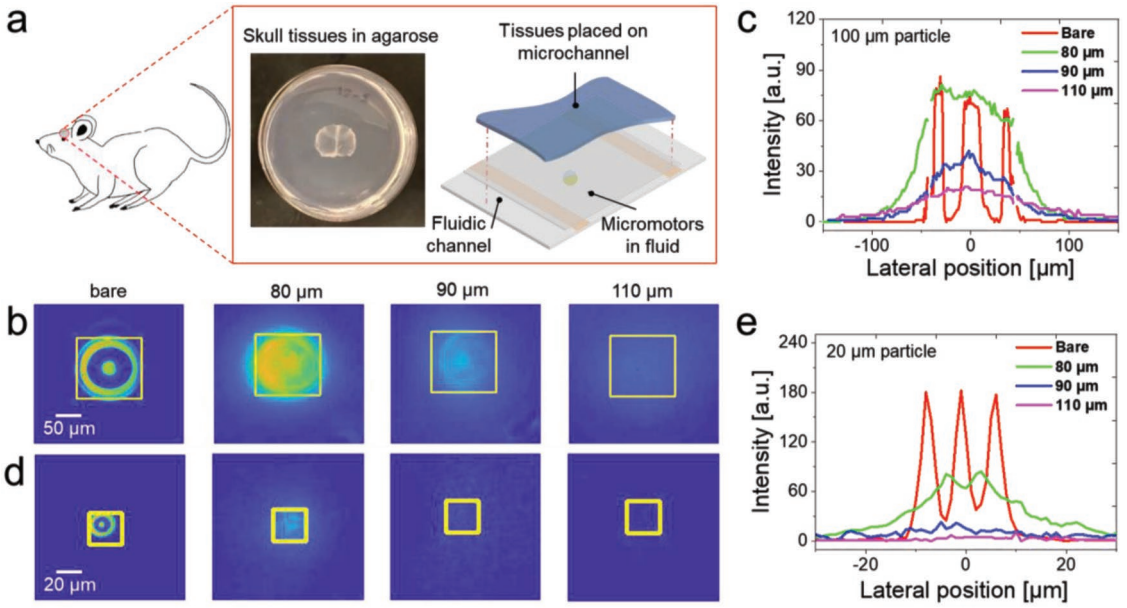

Figure 5. Ex vivo tracking of single micromotors under mice skull tissues: a) Mouse skull tissue preserved in agarose prior to experiments and schematic of the fluidic channel containing the reflective micromotors. b) Tracking of a single micromotor (100 µm in diameter) with varying thicknesses of the mice skull tissues (80–110 µm in thickness). c) Intensity profile of the micromotors (100 µm) beneath varying thicknesses of the skull tissues. d) Tracking of a single micromotor (20 µm in diameter) with varying thicknesses of the skull tissues (80–110 µm in thickness). e) Intensity profile for 20 µm micromotors up to 110 µm deep in tissue.

also hold great potential as remote diagnosis tools, where a biological or physiological parameter can be detected from the outside of the body to determine certain health condition. An example of the potential use of micromotors as active rheometers is the one reported by Fisher's group, which employed magnetic propellers to determine the rheological properties of the vitreous of the eye.[75,76] In this work, we demonstrate the imaging of moving magnetic reflective micromotors to determine the viscosity of various fluids by determining their velocity in real-time (Video S5, Supporting Information). As a proof of concept, we tracked single micromotors (20 and 100 µm in diameter) through different concentrations of methylcellulose (MC) solutions which mimic the rheological properties of a variety of biological fluids (**Figure 6**a). In particular, MC-enriched water solutions (0%, 0.2%, 0.4%, and 0.6%), corresponding to the viscosities of 0.00136, 0.00228, 0.0055, and 0.01114 Pa.s (determined by a conventional rheometer) were used for this experiment. The viscosity of normal whole blood is about 0.004 Pa.s, which is similar to the one obtained by the substitute fluids of MC (0.2–0.4%). Thus, one can envision this method to analyze, e.g., blood viscosity, which is one of the key parameters to diagnose cardio-vascular diseases such as cardio-cerebrovascular diseases, hemorrhagic shock, and so on.[77] Detailed studies are needed and will be carried out in future experiments. For this experiment, a rotating magnetic field was applied to steer the micromotors. We found out that the micromotors move more efficiently under rotating magnetic fields, especially when they are in close contact to surfaces as well as in highly viscous solutions. The movement and the corresponding change in the speed of the different micromotors are presented in Figure 6b. However, in order to measure fluid viscosity, it is also important to keep in mind the influence of the confinement on the micromotor hydrodynamics. For that we fabricated a microchannel with a mimicking vascular network, with three different widths 100, 50, and 25 µm, all with a height of about 50 µm (Figure 6c-i), and as expected when moving the micromotor at 3 mT and 5 Hz, the micromotor speed was reduced when entering different cross-section channels as it can be seen in Figure 6c-ii. This reduction can be attributed to the increased hydrodynamic resistance of small channels, in particular, the ones close to the micromotor size. Reflective micromotors (20 µm) can also carry a therapeutic cargo (doxorubicin hydrochloride, DOX-HCL), a model drug which is widely approved for cancer therapy.[75] For demonstration purposes, we employed the well-known physical adsorption method to load drug onto the microparticles. First, we prepared a solution of DOX-HCL at a concentration of 20 µg mL^{-1} dissolved in water, and incubated the metal-coated silica particles in that solution for 24 h, under agitation and at room temperature (RT). The drug-loaded particles were then washed twice and collected by centrifugation. The drug molecules were adsorbed onto the silica surface as previously reported in literature.[74] To evaluate the loading and transport of the DOX-HCL loaded micromotors, fluorescence microscopy was used to track a single drug-loaded micromotor in the channel with an excitation wavelength of 470 nm (Figure 6d). It was possible to distinguish drug-loaded micromotors from un-loaded ones (control) using fluorescence microscopy. DOX-HCL possesses an intrinsic fluorescence with an emission peak at around 600 nm (Figure 6d-i). Figure 6d-ii shows the navigation of a drug-loaded micromotor within a microfluidic channel.

Still, there is room to improve the presented approach, e.g., using rotational magnetic fields to induce motion through

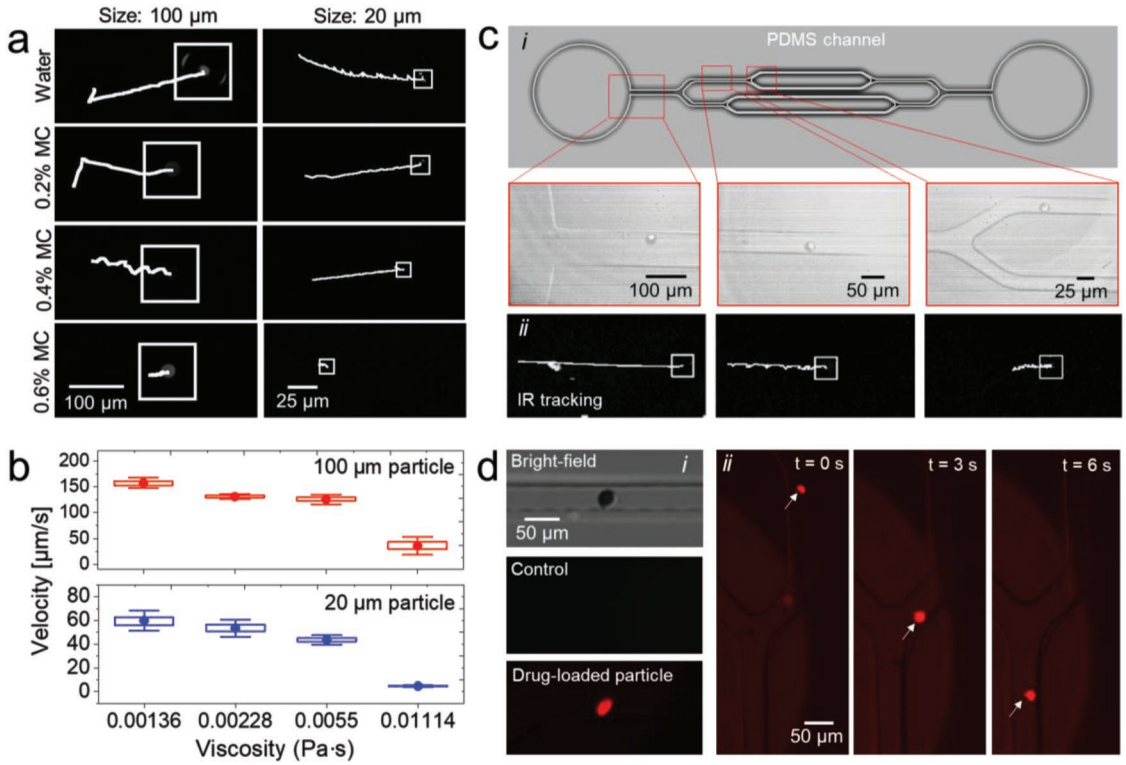

Figure 6. Micromotors moving through viscous fluids and as a drug-carriers: a) Tracking of 100 and 20 µm micromotors through different concentrations of methylcellulose water solutions (0%, 0.2%, 0.4%, and 0.6%). b) Relation between speed and viscosity of fluid for both 20 and 100 µm reflective micromotors. c) i) Schematic of a PDMS microchannel and movement of the 20 µm particle within the same time interval (5 s), and ii) The corresponding tracking by using the IR imaging setup. d) i) Bright-field, control, and fluorescence images of DOX-HCL-loaded micromotors, and the time lapse images of the transported drug-loaded reflective micromotor within the microfluidic network. White arrows show the position of drug-loaded micromotor after different time intervals.

rolling of the reflective micromotors with known frequency (as previously shown) can be beneficial for extracting additional information about the micromotor positioning and speed in deep tissues by precisely sorting out the background noise from the rotating micromotor signal. Additionally, the usage of an IR wavelength in the second biological window could improve the results due to reduced photon scattering, although LED sources at this wavelength range have commonly reduced power. A change to laser light is also possible, however it leads to a speckled illumination of the particle, which can result in an incomplete ring shape and consequently in an increase of processing time.

In in vivo applications, the scattering tissues will not be static, but will be moving, due to the movement of the animal or simply by changes due to the heartbeat, requiring continuous calibration steps. This will lead to motion artifacts. A solution could be to track any change induced by the artifacts and counteract with adaptive optics. Commonly, the adaptive optical control should be at least a factor of five faster than the disturbance. Wavefront shaping approaches like digital optical phase conjugation[78] have been shown to be capable of extending the range of optical techniques into deep-tissue applications of up to several TMFP. They also enable to create minimally invasive needle-sized endoscopes[79] that could be effectively used to get closer to the region of interest. Moreover, hybrid techniques such as optoacoustic imaging seems also promising for deep tissue penetration as it takes the advantages of both optical excitation and ultrasound detection, as it was recently shown by micro-objects tracking.[80] However, these approaches are technically sophisticated and require a complex and bulky setup.

3. Conclusions

In this work, we have demonstrated real-time and high-resolution tracking of single "reflective" micromotors (100 and 20 µm in diameter) through scattering tissues (phantom and ex vivo mouse skull), which are key requisites for translating micromotors to clinical applications. The achievable penetration depth in our current setup depends mainly on the camera properties like the dynamic range and sensitivity, as well as on the employed exposure time, illumination intensity, and field of view. However, using the high reflectivity of micromotors enables the tracking their movement through phantom thicknesses of up to 0.32 TMFP (which corresponds to 160 µm of skull tissue). The presented reflective micromotors have the potential to be used as theranostic tools. They can serve as active microrheometers which by analyzing their motion performance within tissues provide information about physiological fluid viscosities possibly associated with a disease status. Moreover, the micromotors can be loaded with drugs and be

transported precisely within a microfluidic network through rolling thanks to an applied rotating magnetic field. Their precise maneuverability and the capability to use them as a carrier for particle-based assemblies like bacteria-particle, sperm-particle, particulate drug carriers, Janus motors (actuated by for instance internal stimuli or external actuation) open up diverse approaches for sub-skin, small animals and on-chip organ applications.

4. Experimental Section

Materials and Reagents: PDMS was purchased from Dow Corning, GmbH Germany. Glycerol was purchased from Sigma-Aldrich, Germany. SiO_2 microparticles of diameter 100 and 20 µm were purchased from Corpuscular Inc., USA.

Fabrication of Reflective Micromotors: Reflective micromotors were fabricated via a drop casting method and subsequent metallic layers deposition. In detail, glass substrates (25×25 mm^2) were rinsed and ultra-sonicated (Elmasonic, Elma Schmidbauer GmbH) in acetone first and then in isopropanol, and finally dried in a stream of N_2. The glass slides were further treated with oxygen plasma, leading to the removal of impurities and contaminants from the surface (Diener electronics), to obtain clean and hydrophilic substrates. Then, a monolayer of micro-sized (⌀ = 100 and 20 µm, Corpuscular Inc., USA) silicon dioxide (SiO_2) particles was assembled, using the drop casting method. SiO_2 particles were washed with methanol and centrifuged for 1 min to remove supernatant and then again mixed with methanol and well mixed prior drop casting. The micro arrays were randomly formed in the direction of solvent evaporation. Silica particles were mixed thoroughly in methanol and ≈20 µL of particle–solvent solution was drop-casted on the edge of pre-plasma-treated glass slide. The glass slide was adjusted at an angle to allow the spreading of silica particles over the entire glass cover slip, making a homogenous monolayer of silica particles. The resulted monolayer was dried at RT and spacing among SiO_2 particles was controlled by tuning the solution concentration. The samples were coated with Au (50 nm), Ti (10 nm), Fe (30 nm), and Au (50 nm) of high purity (99.995%) by electron beam physical vapor deposition (e-beam evaporator, Plassys MEB550S). Iron (Fe, 30 nm) layer was evaporated for magnetic guidance and titanium (Ti, 10 nm) was chosen as an intermediate adhesive layer sandwiched between gold and iron layers. To obtain reflective micromotors, the sample was coated from one side, and the sample holder was placed at 0° and deposition rate was set to 0.5 Å s^{-1}.

Fabrication of PDMS-Glycerol Phantoms and Fluidic Channel: The phantoms were prepared freshly, and the thickness was controlled by the Vernier caliper. The fabrication of tissue-mimicking phantoms was explained in detail.[72] Briefly, first, the two components of silicone elastomer PDMS (Dow Corning GmbH) were mixed together in quantities of 10:1 parts by volume, a ration of the base PDMS material to the curing agent volumes. Subsequently, glycerol (Sigma-Aldrich, GmbH) in 0.5 parts per volume was included carefully by preventing the excessive amounts of air bubbles. The mixture was thoroughly mixed and poured into petri dishes (Henke Sass, Wolf GmbH) with controlled thicknesses. Air bubbles were evacuated from the mixture in a vacuum chamber. The mixture was left at RT to solidify for 24 h.

Fluidic channels were fabricated by using two-layer parafilm sheets that allowed the tracking of the reflective micromotors in a confined space. A glass slide and a cover slip were sonicated in acetone and isopropanol for 3 min each. The parafilm stripes were placed between glass slide and cover slip and melted at 120 °C to fasten the three parts together, resulting in an enclosed channel.[81]

Optical Setup and Imaging Studies: A straightforward approach was adopted and an IR high-power LED (970 nm, Thorlabs, Germany) was used to illuminate the micromotors with and without scattering phantoms. The light was collimated and directed toward the fluidic channel by the aid of an objective lens (Mitutoyo 20x, Edmund optics). An InGaAs camera (900–1700 nm, Xenics Belgium) was used for image acquisition. A home-made C^{++} code was implemented to drive the camera and to directly process the data by subtracting the scattering background and using image correlation-based algorithms to track the micromotors. 3D micromanipulator (XYZ), beam splitter, and all other optical components and holders were purchased from Thorlabs, GmbH Germany. Microsoft Excel 2013, Origin 2018, MATLAB (intensity spread analysis), and ImageJ software (for tracking and speed measurement of micro-reflectors) were used for the analysis of the experimental data.

Electron beam deposition (Plassys e-beam evaporator) was used to deposit different reflective metallic layers. SEM, optical microscopy, and AFM analysis were conducted for the characterization of the prepared reflective micromotors. SEM (Zeiss Nvision 40, Carl Zeiss Microscopy GmbH) was performed by coating the sample with ≈10 nm Pt to make the specimen conductive and to avoid charging effects during imaging. Bright-field microscopy was performed using an optical microscope (Zeiss Microscopy GmbH) equipped with 5x, 10x, and 20x objective. AFM (dimension icon from Bruker) was used to measure the surface roughness in 2D and 3D surface profile. The roughness of 1 µm^2 area was calculated by the root mean square (R_q = 1.62 nm) and the maximum height feature was measured ranging from −5 to 5 nm.

Mice Skull Tissues: The mice skulls were obtained from the Mortensen Lab at the University of Georgia in Athens, USA, and used in accordance with the care and use of laboratory animals. All mice were anaesthetized before sacrificing using O_2 gas flow mixed with isoflurane. The hair over the scalp was removed using hair removing cream. An incision was made on the mice brains and the skull tissues were removed immediately after sacrificing the mice.

The mice were decapitated after euthanizing with CO_2, the skin and periosteum were removed and fixed in 2% paraformaldehyde for 2 days. The top part of the skull was cut using a dental drill, and washed with phosphate buffered saline (PBS) to remove unwanted tissues. The samples were mounted in agarose gel (Figure 5a) to maintain their optical properties. The thickness of the skull tissues was estimated from laser triangulation measurements. The skull tissues were carefully removed from the agarose gel prior to use, and placed in PBS to prevent dehydration. First, the micromotors (100 µm) were injected into the fluidic channel and aligned by using external magnetic fields.

Supporting Information

Supporting Information is available from the Wiley Online Library or from the author.

Acknowledgements

This work was supported by the German Research Foundation SPP 1726 "Microswimmers-From Single Particle Motion to Collective Behavior". O.G.S. acknowledges financial support by the Leibniz Program of the German Research Foundation. J.W.C. is supported by a Reinhart Koselleck project of the German Research Foundation (DFG, Cz55/30). This work is also part of the projects that have received funding from the European Research Council (ERC) under the European Union's Horizon 2020 research and innovation program (grant agreement no. 835268 and no. 853609). The authors thank Dr. Kayvan Tehrani for preparing the mouse skulls, Barbara Eichler for the AFM analysis, and Carlos Medina for helping with the IR camera interfacing. Finally, the discussions with Dr. Daniil Karnaushenko and Dr. Libo Ma are highly appreciated.

Conflict of Interest

The authors declare no conflict of interest.

Keywords

medical microbots, mice skull tissues, micromotors, micro-reflectors, phantoms, real-time tracking

Received: July 1, 2019
Revised: September 11, 2019
Published online: October 21, 2019

[1] W. F. Paxton, K. C. Kistler, C. C. Olmeda, A. Sen, S. K. St. Angelo, Y. Cao, T. E. Mallouk, P. E. Lammert, V. H. Crespi, *J. Am. Chem. Soc.* **2004**, *126*, 13424.
[2] S. Fournier-Bidoz, A. C. Arsenault, I. Manners, G. A. Ozin, *Chem. Commun.* **2005**, 441.
[3] J. R. Howse, R. A. L. Jones, A. J. Ryan, T. Gough, R. Vafabakhsh, R. Golestanian, *Phys. Rev. Lett.* **2007**, *99*, 48102.
[4] Y. Mei, G. Huang, A. A. Solovev, E. B. Ureña, I. Mönch, F. Ding, T. Reindl, R. K. Y. Fu, P. K. Chu, O. G. Schmidt, *Adv. Mater.* **2008**, *20*, 4085.
[5] A. A. Solovev, Y. Mei, E. B. Ureña, G. Huang, O. G. Schmidt, *Small* **2009**, *5*, 1688.
[6] S. Sanchez, L. Soler, J. Katuri, *Angew. Chem., Int. Ed.* **2015**, *54*, 1414.
[7] R. Dreyfus, J. Baudry, M. L. Roper, M. Fermigier, H. A. Stone, J. Bibette, *Nature* **2005**, *437*, 862.
[8] L. Zhang, J. J. Abbott, L. Dong, B. E. Kratochvil, D. Bell, B. J. Nelson, *Appl. Phys. Lett.* **2009**, *94*, 2007.
[9] A. Ghost, P. Fischer, *Nano Lett.* **2009**, *9*, 2243.
[10] M. Medina-Sánchez, L. Schwarz, A. K. Meyer, F. Hebenstreit, O. G. Schmidt, *Nano Lett.* **2016**, *16*, 555.
[11] W. Wang, L. A. Castro, M. Hoyos, T. E. Mallouk, *ACS Nano* **2012**, *6*, 6122.
[12] D. Kagan, M. J. Benchimol, J. C. Claussen, E. Chuluun-Erdene, S. Esener, J. Wang, *Angew. Chem., Int. Ed.* **2012**, *51*, 7519.
[13] W. Wang, S. Li, L. Mair, S. Ahmed, T. J. Huang, T. E. Mallouk, *Angew. Chem., Int. Ed.* **2014**, *53*, 3201.
[14] M. Liu, T. Zentgraf, Y. Liu, G. Bartal, X. Zhang, *Nat. Nanotechnol.* **2010**, *5*, 570.
[15] Z. Wu, X. Lin, Y. Wu, T. Si, J. Sun, Q. He, *ACS Nano* **2014**, *8*, 6097.
[16] D. B. Weibel, P. Garstecki, D. Ryan, W. R. DiLuzio, M. Mayer, J. E. Seto, G. M. Whitesides, *Proc. Natl. Acad. Sci. U. S. A.* **2005**, *102*, 11963.
[17] V. Magdanz, S. Sanchez, O. G. Schmidt, *Adv. Mater.* **2013**, *25*, 6581.
[18] H. Xu, M. Medina-Sánchez, V. Magdanz, L. Schwarz, F. Hebenstreit, O. G. Schmidt, *ACS Nano* **2018**, *12*, 327.
[19] L. Schwarz, M. Medina-Sánchez, O. G. Schmidt, *Appl. Phys. Rev.* **2017**, *4*, 031301.
[20] M. Guix, S. M. Weiz, O. G. Schmidt, M. Medina-Sánchez, *Part. Part. Syst. Charact.* **2018**, *35*, 1700382.
[21] B. E.-F. de Ávila, P. Angsantikul, J. Li, M. Angel Lopez-Ramirez, D. E. Ramírez-Herrera, S. Thamphiwatana, C. Chen, J. Delezuk, R. Samakapiruk, V. Ramez, L. Zhang, J. Wang, *Nat. Commun.* **2017**, *8*, 272.
[22] D. Patra, S. Sengupta, W. Duan, H. Zhang, R. Pavlick, A. Sen, *Nanoscale* **2013**, *5*, 1273.
[23] R. Fernandes, D. H. Gracias, *Adv. Drug Delivery Rev.* **2012**, *64*, 1579.
[24] F. Mou, C. Chen, Q. Zhong, Y. Yin, H. Ma, J. Guan, *ACS Appl. Mater. Interfaces* **2014**, *6*, 9897.
[25] Z. Hosseinidoust, B. Mostaghaci, O. Yasa, B.-W. Park, A. V. Singh, M. Sitti, *Adv. Drug Delivery Rev.* **2016**, *106*, 27.
[26] A. C. Hortelão, T. Patiño, A. Perez-Jiménez, À. Blanco, S. Sánchez, *Adv. Funct. Mater.* **2018**, *28*, 1705086.
[27] O. Felfoul, M. Mohammadi, S. Taherkhani, D. De Lanauze, Y. Zhong Xu, D. Loghin, S. Essa, S. Jancik, D. Houle, M. Lafleur, L. Gaboury, M. Tabrizian, N. Kaou, M. Atkin, T. Vuong, G. Batist, N. Beauchemin, D. Radzioch, S. Martel, *Nat. Nanotechnol.* **2016**, *11*, 941.
[28] Y. Tu, F. Peng, A. A. M. André, Y. Men, M. Srinivas, D. A. Wilson, *ACS Nano* **2017**, *11*, 1957.
[29] S. K. Srivastava, M. Medina-Sánchez, B. Koch, O. G. Schmidt, *Adv. Mater.* **2016**, *28*, 832.
[30] G. W. Rogers, *AIP Conf. Proc.* **2012**, *1433*, 705.
[31] B. J. Nelson, I. K. Kaliakatsos, J. J. Abbott, *Annu. Rev. Biomed. Eng.* **2010**, *12*, 55.
[32] B. Esteban-Fernández de Ávila, M. A. Lopez-Ramirez, D. F. Báez, A. Jodra, V. V Singh, K. Kaufmann, J. Wang, *ACS Sens.* **2016**, *1*, 217.
[33] R. C. McGlennen, *Clin. Chem.* **2001**, *47*, 393 LP.
[34] M. Medina-Sánchez, O. G. Schmidt, *Nature* **2017**, *545*, 406.
[35] D. Vilela, U. Cossío, J. Parmar, A. M. Martínez-Villacorta, V. Gómez-Vallejo, J. Llop, S. Sánchez, *ACS Nano* **2018**, *12*, 1220.
[36] A. Sánchez, V. Magdanz, O. G. Schmidt, S. Misra, in *Proc. IEEE RAS EMBS Int. Conf. Biomed. Robot. Biomechatronics*, IEEE, Piscataway, NJ **2014**, p. 169.
[37] Z. Xu, M. Chen, H. Lee, S.-P. Feng, J. Y. Park, S. Lee, J. T. Kim, *ACS Appl. Mater. Interfaces* **2019**, *11*, 15727.
[38] B. W. Park, J. Zhuang, O. Yasa, M. Sitti, *ACS Nano* **2017**, *11*, 8910.
[39] J. Li, S. Thamphiwatana, W. Liu, B. Esteban-Fernández De Ávila, P. Angsantikul, E. Sandraz, J. Wang, T. Xu, F. Soto, V. Ramez, X. Wang, W. Gao, L. Zhang, J. Wang, *ACS Nano* **2016**, *10*, 9536.
[40] A. Servant, F. Qiu, M. Mazza, K. Kostarelos, B. J. Nelson, *Adv. Mater.* **2015**, *27*, 2981.
[41] X. Yan, Q. Zhou, M. Vincent, Y. Deng, J. Yu, J. Xu, T. Xu, T. Tang, L. Bian, Y.-X. J. Wang, K. Kostarelos, L. Zhang, *Sci. Rob.* **2017**, *2*, eaaq1155.
[42] M. J. Paulus, S. S. Gleason, S. J. Kennel, P. R. Hunsicker, D. K. Johnson, *Neoplasia* **2000**, *2*, 62.
[43] L. Convert, R. Lebel, S. Gascon, R. Fontaine, J.-F. Pratte, P. Charette, V. Aimez, R. Lecomte, *J. Nucl. Med.* **2016**, *57*, 1460.
[44] X. Yan, Q. Zhou, M. Vincent, Y. Deng, J. Yu, J. Xu, T. Xu, T. Tang, L. Bian, Y.-X. X. J. Wang, K. Kostarelos, L. Zhang, *Sci. Robot.* **2017**, *2*, eaaq1155.
[45] V. Ntziachristos, *Nat. Methods* **2010**, *7*, 603.
[46] S. Gigan, *Nat. Photonics* **2017**, *11*, 14.
[47] A. Jabłoński, *Nature* **1933**, *131*, 839.
[48] C. Eggeling, J. Widengren, R. Rigler, C. A. M. Seidel, *Anal. Chem.* **1998**, *70*, 2651.
[49] M. Grabolle, J. Ziegler, A. Merkulov, T. Nann, U. Resch-Genger, *Ann. N. Y. Acad. Sci.* **2008**, *1130*, 235.
[50] J. Jiao, Z.-J. Zhou, W.-H. Zhou, S.-X. Wu, *Mater. Sci. Semicond. Process.* **2013**, *16*, 435.
[51] Y. Tsukasaki, M. Morimatsu, G. Nishimura, T. Sakata, H. Yasuda, A. Komatsuzaki, T. M. Watanabe, T. Jin, *RSC Adv.* **2014**, *4*, 41164.
[52] V. Biju, T. Itoh, A. Anas, A. Sujith, M. Ishikawa, *Anal. Bioanal. Chem.* **2008**, *391*, 2469.
[53] Y. Zhang, G. Hong, Y. Zhang, G. Chen, F. Li, H. Dai, Q. Wang, *ACS Nano* **2012**, *6*, 3695.
[54] C. Li, Y. Zhang, M. Wang, Y. Zhang, G. Chen, L. Li, D. Wu, Q. Wang, *Biomaterials* **2014**, *35*, 393.
[55] Y. Zhang, Y. Liu, C. Li, X. Chen, Q. Wang, *J. Phys. Chem. C* **2014**, *118*, 4918.
[56] P. Jiang, C.-N. Zhu, Z.-L. Zhang, Z.-Q. Tian, D.-W. Pang, *Biomaterials* **2012**, *33*, 5130.
[57] S. J. Rosenthal, J. C. Chang, O. Kovtun, J. R. McBride, I. D. Tomlinson, *Chem. Biol.* **2011**, *18*, 10.
[58] N. Genicio, J. Gallo Paramo, A. J. Shortt, *Invest. Ophthalmol. Visual Sci.* **2015**, *56*, 3051.

[59] Y.-P. Chang, F. Pinaud, J. Antelman, S. Weiss, *J. Biophotonics* **2008**, *1*, 287.
[60] P. Gladyshev, V. Kouznetsov, C. M. Bonilla, S. Dezhurov, D. Krilsky, A. Vasiliev, O. Morenkov, V. Vrublevskaya, P. Tsygankov, S. Ibragimova, A. Rybakova, *IOP Conf. Ser.: Mater. Sci. Eng.* **2016**, *151*, 012042.
[61] Y. D. Han, H. S. Kim, Y. M. Park, H. J. Chun, J. H. Kim, H. C. Yoon, *ACS Appl. Mater. Interfaces* **2016**, *8*, 10767.
[62] J. Zhang, J. Liu, L. M. Wang, Z. Y. Li, Z. Yuan, *J. Biophotonics* **2017**, *10*, 878.
[63] E. T. K. Demann, P. S. Stein, J. E. Haubenreich, *J. Long-Term Eff. Med. Implants* **2005**, *15*, 687.
[64] R. Shukla, V. Bansal, M. Chaudhary, A. Basu, R. R. Bhonde, M. Sastry, *Langmuir* **2005**, *21*, 10644.
[65] S. Zingler, R. Erber, C. J. Lux, R. Seeberger, D. Bister, *Oral Surg., Oral Med., Oral Pathol. Oral Radiol.* **2013**, *116*, 159.
[66] J. H. Fan, W. I. Hung, W. T. Li, J. M. Yeh, in *IFMBE Proceedings* **2009**, *23*, 870.
[67] A. Steyerl, S. S. Malik, L. R. Iyengar, *Phys. B* **1991**, *173*, 47.
[68] M. D. Stoudt, K. Vedam, *Appl. Opt.* **1978**, *17*, 1855.
[69] C. Mattsson, J. O. Cavallin, *Oikos* **1972**, *23*, 285.
[70] O. Loebich, *Gold Bull.* **1972**, *5*, 2.
[71] M. M. Stanton, J. Simmchen, X. Ma, A. Miguel-López, S. Sánchez, *Adv. Mater. Interfaces* **2016**, *3*, 1500505.
[72] M. S. Wróbel, A. P. Popov, A. V. Bykov, V. V. Tuchin, M. Jędrzejewska-Szczerska, *Biomed. Opt. Express* **2016**, *7*, 2088.
[73] ICNIRP, *Health Phys.* **2013**, *71*, 804.
[74] S. L. Jacques, *Phys. Med. Biol.* **2013**, *58*, 5007.
[75] O. Tacar, P. Sriamornsak, C. R. Dass, *J. Pharm. Pharmacol.* **2013**, *65*, 157.
[76] T. Qiu, D. Schamel, A. G. Mark, P. Fischer, in *Proc. – IEEE Int. Conf. Robotics and Automation*, Institute of Electrical and Electronics Engineers Inc., Piscataway, NJ **2014**, 3801.
[77] G. Chen, L. Zhao, Y. Liu, F. Liao, D. Han, H. Zhou, *Chin. Sci. Bull.* **2012**, *57*, 1946.
[78] N. Koukourakis, B. Fregin, J. König, L. Büttner, J. W. Czarske, *Opt. Express* **2016**, *24*, 22074.
[79] R. Kuschmierz, E. Scharf, N. Koukourakis, J. W. Czarske, *Opt. Lett.* **2018**, *43*, 2997.
[80] A. Aziz, M. Medina-Sánchez, J. Claussen, O. G. Schmidt, *Nano Lett.* **2019**, *19*, 6612.
[81] M. Medina-Sánchez, M. Guix, S. Harazim, L. Schwarz, O. G. Schmidt, in *2016 Int. Conf. Manip. Autom. Robot. Small Scales, MARSS*, IEEE, Piscataway, NJ **2016**, pp. 1–6.